TUDelft

Delft University of Technology

Adsorption of molybdenum on Zr-based MOFs for potential application in the ^{99}Mo/^{99m}Tc generator

Ma, Chao; Vasileiadis, Alexandros; Wolterbeek, Hubert T.; Denkova, Antonia G.; Serra Crespo, Pablo

Important note
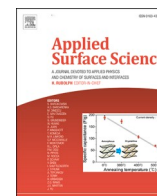To cite this publication, please use the final published version (if applicable).
Please check the document version above.

Full Length Article

Adsorption of molybdenum on Zr-based MOFs for potential application in the ^{99}Mo/^{99m}Tc generator

Chao Ma [a], Alexandros Vasileiadis [b], Hubert T. Wolterbeek [a], Antonia G. Denkova [a,*], Pablo Serra Crespo [a,*]

[a] *Applied Radiation and Isotopes, Radiation Science and Technology, Faculty of Applied Sciences, Delft University of Technology, 2629 JB Delft, Mekelweg 15, the Netherlands*
[b] *Storage of Electrochemical Energy, Radiation Science and Technology, Faculty of Applied Sciences, Delft University of Technology, 2629 JB Delft, Mekelweg 15, the Netherlands*

ABSTRACT

The potential of the metal–organic framework UiO-66 and its functionalized derivatives for their utilization in the ^{99}Mo/^{99m}Tc generator was assessed. Molybdenum adsorption experiments, structure characterization, molecular simulations and column experiments with molybdenum-99 were carried out. The results showed that the maximum molybdenum adsorption capacity achieved for UiO-66 was 335 mg g^{-1}. Adsorption on the surface of the UiO-66 occurs via electrostatic interaction and DFT calculations verified the enhanced affinity between the adsorbents and the molybdenum ions by Zr-O-Mo coordination, anion-π as well as hydrogen bonds. In addition, the performance of a ^{99}Mo/^{99m}Tc generator fabricated with Form-UiO-66 was evaluated. The results showed that adsorption was comparable with the experiments using non-active molybdenum and that the ^{99m}Tc elution efficiency of around 70% could be achieved without zirconium breakthrough.

1. Introduction

Technetium-99 m (^{99m}Tc) is the most often used radionuclide due to its application in organ perfusion, tumour imaging and bone scanning, among others, with around 40 million diagnostic procedures per year [1]. The main reasons for ^{99m}Tc ubiquitous utilization are its decay characteristics, which include the relatively low γ-ray energy, a short half-life (6.1 h), but also its rich chemistry and a wide availability via the ^{99}Mo/^{99m}Tc generator [2,3]. Nowadays, the ^{99}Mo production is based on the fission of enriched uranium-235 target, which is irradiated in a limited number of nuclear reactors [4,5]. On top of that, most of nuclear reactors are at end of their operational life and need regular maintenance, causing serious problems for the supply of ^{99}Mo [6]. For example, the reactors in Canada and the Netherlands shut down unexpectedly for a considerable time in 2008, resulting in a significant decrease worldwide of ^{99}Mo availability [7,8]. In addition, a low yield of only about 6% is obtained and therefore enormous nuclear waste is produced during this process [9]. To overcome those disadvantages, several alternative production routes have been proposed. However, compared with uranium-235 fission, all the alternative routes deliver ^{99}Mo of much lower specific activity (LSA), preventing the preparation of ^{99}Mo/^{99m}Tc generators with sufficient activity [10]. In order to use such LSA ^{99}Mo, the adsorption capacity of the generators needs to be considerably increased.

The conventional bulk adsorbent utilized in the generator column is alumina (Al_2O_3) because of its high thermal stability, chemical stability, radiation stability and affinity towards molybdenum. However, alumina has a rather low molybdenum adsorption capacity ranging from 2 to 20 mg g^{-1} [11]. In an attempt to improve the adsorption capacity, a variety of materials having nano-dimensions or mesoporous structures were investigated as adsorbents due to their large pore volume and high surface area. For example, Saptiama et al.[12] reported the fabrication of mesoporous alumina spheres using post-synthesis water–ethanol treatment and reaching Mo adsorption capacity of 56.2 mg g^{-1} at pH 3. Denkova et al.[13] utilized Al-TUD-1 having high surface area and achieved a maximum adsorption capacity of 112 mg g^{-1}. Chakravarty et al.[14] synthesized nanocrystalline Al_2O_3 with average crystallite size 2–3 nm using a template method resulting in very high adsorption capacity in the order of 225 ± 20 mg g^{-1} when applying a double column design. Although these studies are very promising, the obtained

adsorption capacities are still insufficient to be applied to LSA ^{99}Mo produced by most of the production routes, leaving a room for further improvement.

Very promising materials are the so-called metal–organic frameworks (MOFs) which have received wide attention in many applications including gas capture [15–17], catalysis [18,19], wastewater treatment [20,21], drug delivery [22–25], and others [26–28]. Compared with traditional porous materials, MOFs exhibit large surface area, high porosities, versatile structures and easy functionalization [29]. However, the degradation of some MOFs in water or extreme environment limits their industrial applications [30,31]. Recently, a zirconium-based MOF, UiO-66, was researched extensively as an adsorbent due to its water stability, excellent chemical and thermal stability [32–34]. Furthermore, it demonstrated that hydroxyl groups play an important role in molybdenum adsorption based on previous reports [12,35], which is why this material was selected in this research.

In this work, the UiO-66 and its functionalized derivatives were synthesized and characterized and their molybdenum adsorption properties were investigated at different molybdenum concentrations. To understand the interaction pathway between the adsorbent and the molybdenum species, the adsorption mechanism was researched using FT-IR, X-ray photoelectron spectra and DFT simulations. Finally, the synthesized Form-UiO-66 was used for the fabrication of ^{99}Mo/^{99m}Tc generators and its ^{99m}Tc elution performance was evaluated.

2. Materials and methods

2.1. Synthesis and characterization of UiO-66 derivatives

The UiO-66 and its derivatives were synthesized using terephthalate, 2-nitroterephthalic acid and 2-aminoterephthalic acid as ligands based on previously reported methods [32,36]. The detailed descriptions of the synthesized processes are presented in the Supporting Information (S-2).

Powder X-ray diffraction measurements were performed on a PANalytical X'Pert Pro pw3040/60 diffractometer with Cu Kα radiation operating at 45 kV and 40 mA. Nitrogen adsorption isotherms were obtained using a Micromeritics Tristar II at 77 K and the BET surface area was calculated at a relative pressure range between 0.05 and 0.15. Before the measurement, samples were degassed under vacuum at 200 °C for 16 h. Surface morphology was recorded by a field emission scanning electron microscopy (SEM, JSM-7001F) and elemental composition was collected with an energy dispersive spectrometer (EDS, JEOL ISM-IT100). Fourier transform infrared spectroscopy (FT-IR) were collected over a range of 400–4000 cm^{-1} using a NICOLET 6700 and samples were dispersed in KBr and pellets with a diameter of 10 mm were made. The molybdenum concentrations before and after adsorption were measured using inductive coupled plasma optical emission spectrometry (ICP-OES, Optima 4300 DV, Perkin Elmer). 1 mg of powder sample was dispersed in 2 mL of solution with a pH range of 2–12 and the pH of the solution was adjusted using NaOH and HCl solutions. The Zeta potential of the suspension was measured using a Malvern ZetaSizer nano-ZS instrument. X-ray photoelectron spectra (XPS) of UiO-66 were performed by Thermofisher Scientific electron spectroscopy with K-alpha surfaces analysis.

2.2. Molybdenum adsorption

The adsorption capacity of molybdenum on Zr-based MOFs was determined by dispersing the powder in solutions of different molybdenum concentrations. The change in concentration before and after the addition of MOFs determines the amount of molybdenum adsorbed. First, a molybdenum solution (20 mg mL^{-1}) was prepared by dissolving MoO$_3$ into NaOH solution (1 M) and the pH of the solution was adjusted to 3.00 ± 0.03 by adding HCl. Then the prepared molybdenum solution was diluted into different concentrations range from 0.1 mL to 20 mL

using Mili-Q water. The Mo adsorption of all the adsorbents was determined by batch equilibration experiments. An accurately weighed amount of adsorbent (circa 10 mg) was added into 1 mL Mo solution at a certain concentration and shaken at room temperature for 16 h with a speed of 1200 rpm. Adsorption isotherms were determined in a Mo concentration range from 0.1 to 20 mg mL^{-1}. The concentrations of the solution before and after absorption were measured by ICP-OES and all tests were conducted in triplicate at room temperature. The static adsorption capacity was calculated by the following equation:

$$q_e = \frac{(C_0 - C_e) \times V}{m}$$

where C$_e$ and C$_0$ were molybdenum concentrations at the equilibrium and before adsorption, respectively; V was the volume of solution (mL) and m was the weight of adsorbent (g). Moreover, the Teflon column in ^{99}Mo/^{99m}Tc generator was prepared as shown in the schematic diagram in Fig. S1. Then, 24 mL of ^{99}Mo solution with a concentration of 10 mg mL^{-1} was passed through the column at a flow rate of 0.05 mL min^{-1} and the dynamic adsorption capacity was calculated. After loading ^{99}Mo, the column was rinsed with 100 mL of saline solution to remove the loosely adsorbed molybdenum ions and the practical dynamic adsorption capacity was subsequently determined. Finally, the elution performance of the generator was assessed over a period of 6 days. More details about practical dynamic adsorption capacity and radiochemistry purity were described in the Supporting Information (S-3).

2.3. DFT

Spin-polarised DFT calculations with the PBE exchange–correlation functional [37], as implemented in the plane wave Vienna *Ab initio* Simulation Package (VASP) [38], were performed. A high energy cut-off of 520 eV along with a 3x3x3 Monkhorst-Pack k-point set was selected. Valence-core interactions were probed with the projector augmented wave (PAW) [39] approach considering 4, 1, 6, 12, and 14 valence electrons for C, H, O, Zr, and Mo respectively. In order to account for Van der Walls interactions, the zero damping DFT-D3 method of Grimme et al. [40] was applied in all calculations. Probing the molecular and atomic interactions between the molybdenum species and the host MOF structure was achieved by determining the binding energy, calculated according to the following formula:[41,42]

$$E_B = E_{MH} - E_M - E_H$$

where E$_M$ is the total energy of the molybdenum species isolated in a 25 × 25 × 25 Å^3 vacuum box, E$_H$ is the total energy of the host structure (MOF), and E$_{MH}$ is the total energy of the adsorbed system (molybdenum species and host). Based on the definition of the binding energy provided above, a more negative value indicates stronger binding between the molybdenum species and the MOF. All the relevant structures were geometrically optimized, allowing relaxation of atomic positions, cell shape and volume during the calculation. The total energies were obtained from subsequent self-consistent calculations.

3. Results and discussion

3.1. Structural characterization

The crystal structure of as-prepared Zr-based MOFs was examined by X-ray diffraction and the results can be found in Fig. 1a. It can be observed that all synthesized samples exhibit the characteristic diffraction peaks of UiO-66, indicating that the other three derivative frameworks are isostructural with UiO-66. However, the intensities of UiO-66-NH$_2$ and UiO-66-NO$_2$ are lower, indicating less crystallinity.

Fig. 1b displays FT-IR spectroscopy of UiO-66 and its derivatives as synthesized. A broad band seen at 3421 cm^{-1} for all the materials is assigned to the stretching modes of O-H, which is attributed to the
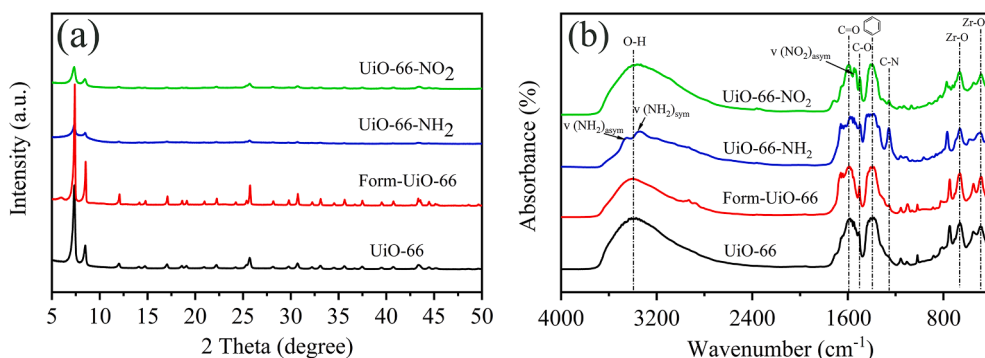
Fig. 1. (a) XRD patterns and (b) FT-IR spectra of UiO-66 and its derivatives before molybdenum adsorption.

adsorbed water on the surface of the samples [43]. The band near 1583 cm^{-1} and 1397 cm^{-1} for all samples can be ascribed to the stretching vibration of C═O on the BDC and the vibration of a benzene ring, respectively [36,44]. The small bands at 485 cm^{-1}, 665 cm^{-1} and 748 cm^{-1} represent the Zr—O and Zr—O_2 stretching vibrations [45]. For the UiO-66-NH_2, the amino group shows absorption bands at 3354 cm^{-1} and 3476 cm^{-1} because of symmetric and asymmetric N—H stretching modes [32]. The appearance of a band at 1549 cm^{-1} can be attributed to the asymmetric stretching mode of NO_2 [46]. Furthermore, the band at 1257 cm^{-1} in the UiO-66-NH_2 and UiO-66-NO_2 particles are due to the C—N stretching absorption mode, suggesting the successful introduction of —NH_2 and —NO_2 groups [47].

Fig. 2a shows the N_2 adsorption isotherm of UiO-66, UiO-66-NH_2, Form-UiO-66 and UiO-66-NO_2 at 77 K. The surface area and pore volumes of all materials were calculated, as shown in Table S1. Non-functionalized UiO-66 and Form-UiO-66 have the largest surface area and pore volumes. Their specific surface areas are 1624 m^2 g^{-1} and 1653 m^2 g^{-1}, whereas the total pore volumes are 0.59 m^3 g^{-1} and 0.61 m^3 g^{-1}, respectively. Materials functionalized with amino (UiO-66-NH_2) and nitro groups (UiO-66-NO_2) have a lower surface area and pore volumes than the non-functionalized counterparts UiO-66s (as shown in Table S1). Besides, the UiO-66-NO_2 exhibited an IV-type adsorption isotherm with a hysteresis cycle. This occurrence could be caused by aggregated small nanoparticles forming large aggregates, generating voids with different sizes within the granules, which is consistent with the SEM micrographs (Fig. S2d).

The pH has an essential influence on molybdenum adsorption, since it affects not only the different molybdenum species present, but also the surface charge of the adsorbents. It has been reported that at pH < 2 the dominant species is $Mo_7O_{24}^{3-}$; while $Mo_7O_{24}^{6-}$ and $Mo_8O_{28}^{4-}$ exist as the main species at pH 2–5 and MoO_4^{2-} predominates pH at >6 [48]. To determine the surface charge of the adsorbents, the zeta potential of all samples was measured in the pH range of 2 to 12, as shown in Fig. 2b. It can be observed that the isoelectric points (IEP) of all the samples are located between pH of 8 and 10, which is similar to alumina. When the

pH is below its IEP, the material is positively charged facilitating its interaction with molybdenum species that are negatively charged through electrostatic forces. When the pH is above the IEP, all samples have negative surface charges that will cause the electrostatic repulsion towards Mo anions. Therefore, the following molybdenum adsorption experiments were carried out under an acidic environment so that adsorption can be enhanced.

3.2. Molybdenum adsorption

The molybdenum adsorption isotherms of UiO-66 MOFs were investigated under different molybdenum concentrations at room temperature, as shown in Fig. 3. As can be seen, molybdenum adsorption on all adsorbents displayed a fast increase and their molybdenum uptake is about 150 mg g^{-1} at relative low molybdenum concentration, which may be attributed to the strong interaction between adsorbents and molybdenum species. With molybdenum concentration increasing, the increase in adsorption capacity slowed down until reaching equilibrium. Finally, the saturated capacity of UiO-66-NH_2, UiO-66-NO_2, Form-UiO-66 and UiO-66 can reach up to 142 mg g^{-1}, 225 mg g^{-1}, 293 mg g^{-1} and
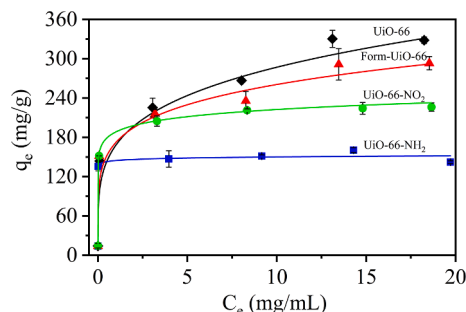

Fig. 3. Mo adsorption isotherms of UiO-66 (black), UiO-66-NH_2(blue), Form-UiO-66 (red) and UiO-66-NO_2 (green) at pH 3.
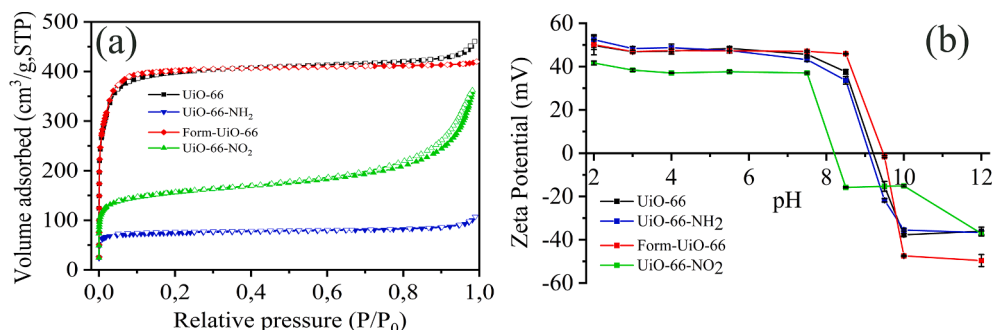

Fig. 2. (a) N_2 adsorption-desorption isotherms and (b) zeta potential of UiO-66 and its derivatives.

334 mg g^{-1}, respectively. The molybdenum uptake in UiO-66 showed the highest adsorption capacity, which is two times larger than that for UiO-66-NH$_2$.

To better understand the molybdenum adsorption on those adsorbents, the adsorption isotherms were linearly fitted using the Langmuir and Freundlich model. All calculated parameters of the two models are displayed in Table S2. As exhibited in Fig. S3, the linear fit of the experimental data using the Langmuir model showed a better fit with higher correlation coefficients (R^2 > 96.5%) than the Freundlich model (Fig. S4). The model displays that the maximum adsorption capacity of UiO-66, UiO-66-NH$_2$, Form-UiO-66 and UiO-66-NO$_2$ are 335 mg g^{-1}, 131 mg g^{-1}, 296 mg g^{-1} and 227 mg g^{-1}, respectively, which are consistent with adsorption isotherms. The relatively low adsorption capacity for UiO-66-NH$_2$ and UiO-66-NO$_2$ may be related to their relatively low surface area and their lower crystallinity. In Table 1, the adsorption capacity of Zr-based MOFs is compared to the Mo adsorption capacity on various other reported materials, showing the outstanding adsorption performance of UiO-66 MOFs.

3.3. Molybdenum adsorption mechanism

To understand the interaction between the molybdenum species and the adsorbents, the MOFs adsorbents were further analyzed by XRD, FT-IR and EDS. In Fig. S5, the XRD patterns show that all adsorbents retain good crystallinity and structure after molybdenum adsorption, as no shifts in the peak positions are observed. However, the relative intensities of the peaks are weakened after molybdenum adsorption, which may be due to trapped molybdenum species on the surface of the adsorbents leading to diminished X-ray contrast between pore cages and porous framework [55]. The EDS mappings (Fig. S6) display uniform distribution of Mo, which suggests that molybdenum is homogeneously adsorbed in the materials. Moreover, the FT-IR spectra (Fig. S7) of UiO-66 MOFs after adsorption shows two new peaks appearing at 948 cm^{-1} and 889 cm^{-1}, which are assigned to the vibration of the Mo=O stretching and Mo-O-Mo stretching of Mo species [56].

The chemical composition and oxidation states of UiO-66 with the best adsorption performance before and after Mo adsorption were analyzed by XPS. As shown in Fig. 4a, the XPS survey indicates the elements of C, O, Zr exist in the samples. The Mo 3d spectra of UiO-66 are presented in Fig. 4b. Two peaks for Mo 3d$_{5/2}$ and Mo 3d$_{3/2}$ are located at 231.8 and 234.9 eV, respectively. The gap of 3.1 eV between two peaks indicates a Mo^{6+} oxidation state [57,58]. The C 1s spectra (Fig. 4c) of UiO-66 before adsorption can be deconvoluted into three peaks, which

are assigned to C=C (284.0 eV), C—C/C—H (284.3 eV) and O—C=O (288.1 eV) [59]. However, the peak of C—H/C—C for UiO-66 after adsorption shifts to 284.7 eV, which indicates the chemical environment of C—H/C—C was changed after loading Mo species. This might be attributed to the different electron density near C-H/C-C in the pores due to the presence of Mo species. In Fig. 4d, the binding energy of Zr 3d exhibits two peaks corresponded to Zr 3d$_{5/2}$ and Zr 3d$_{3/2}$. After molybdenum adsorption, the peak of Zr 3d$_{5/2}$ shifts from 181.99 eV to 182.24 eV and the peak of Zr 3d$_{3/2}$ shifts from 184.36 eV to 184.6 eV. The shift of binding energy towards higher energy may be due to the coordination between Mo species and Zr clusters, causing the change of electron density of Zr [60,61]. This behavior suggests an electronic interaction between Mo species and Zr-O clusters.

To further elucidate the interaction mechanism between Mo species and UiO-66 MOFs, DFT calculations were conducted to investigate the adsorption properties of molybdenum species on the Zr-based MOFs. From the wide variety of the potential Mo(VI) species that exist, depending on the pH, we examined the following representative molecules, H$_2$MoO$_4$, MoO$_4$$^{2-}$ and Mo$_7$O$_{24}$$^{6-}$ (Fig. S8). Mononuclear species of molybdenum exists when molybdenum concentration is lower than 10^{-4} M. Polynuclear molybdenum species can be formed when molybdenum concentration is higher than 10^{-4} M. Mo$_7$O$_{24}$$^{6-}$ is the main species at pH 3–4 when molybdenum concentration is larger than 10^{-3} M [62]. Furthermore, five possible adsorption sites were chosen for inner-sphere calculation, including Zr on clusters (A), O—H groups (B), benzene rings (C), arene C—H groups (D) and the —NH$_2$ or —NO$_2$ groups (E), as shown in Fig. 5. Therefore, five possible molecular interactions were conducted for DFT calculations: coordination between Zr on clusters and the oxygen of Mo species [63], interaction between hydroxyl groups and the oxygen of Mo species [64], the π-anion interaction between Mo anions and benzene rings [65], and hydrogen bond formation between Mo anions and arene C—H groups/—NH$_2$/NO$_2$ [66]. According to the definition provided in the computational method section, negative energy indicates favourable adsorption and the calculated energies are summarized in Table 2.

For UiO-66, the adsorption of MoO$_4$$^{2-}$ species had high interaction energy on positions A (−141 kJ mol^{-1}) and B (−130 kJ mol^{-1}). The configurational environments are shown in Fig. 6. The optimal configurations between Zr nodes and MoO$_4$$^{2-}$ species showed the Zr—O formation with a distance of 1.99 Å (Fig. 6a). This connection near the Zr-clusters caused the change of electron density of the Zr-clusters, which is consistent with the analysis of the Zr 3d spectra of UiO-66. Additionally, our calculations predict that the MoO$_4$$^{2-}$ species can capture the hydrogen atom of the Zr-core (position B), forming HMoO$_4$$^-$ (Fig. 6b). The newly formed molecule stabilizes at a distance of about 1.88 Å from the pore walls. The adsorption site D showed relatively low adsorption energy (−25 kJ mol^{-1}) and formed hydrogen bonds of 2.15–2.18 Å, which is why the binding energy of C-H moved 0.4 eV in XPS spectra of C 1s (Fig. 4c). However, the value of adsorption energy for the C site is positive, indicating unfavourable adsorption. Therefore, the adsorption ability for UiO-66 follows the A < B < D < C order. This behaviour, as mentioned above, is consistent with the UiO-66-NH$_2$ host that shows the order of A < B < E < D < C. As shown in Table 2, the nitrogen environment of the UiO-66-NH$_2$ structure offers an additional adsorption site with strong binding energies. For adsorption near the NH$_2$ environment, we scanned more than 12 different conformers, generally revealing two distinct environments for favourable binding (−73/−50 kJ mol^{-1}), related to the orientation of the molecule. The binding oxygen of the MoO$_4$$^{2-}$ species prefers to be aligned with the plane formed by the NH$_2$ linker, acquiring lower energies (Fig. 6f).

Strong stable binding for the neutral H$_2$MoO$_4$ species occurs near the hydrogen atom of the Zr cluster (position B), where one of the two hydrogen-free oxygens of the adsorbent binds to the hydrogen of the cluster at a distance of 1.75 Å. The rest of the adsorption sites offer an almost equivalent environment for adsorption with binding energies around −65 kJ mol^{-1} (Fig. S9), revealing a relatively flat energy

Table 1
Comparison of the static Mo adsorption capacity of the as-synthesized MOFs with other adsorbent materials.

| Samples	Mo adsorption capacity (mg g^{-1})	Surface area (m^2 g^{-1})	Ref.
TUD-1	112	402	[13]
Hydrous MnO$_2$	50	–	[49]
Hydrous TiO$_2$	230	–	[50]
Al-dropped mesoporous SiO$_2$	16.8	463	[51]
Nano-crystalline titania	141±2	320	[52]
Mesoporous γ-Al$_2$O$_3$	56.2	251	[12]
Nanocrystalline γ-Al$_2$O$_3$	200	252	[11]
PZC	270	–	[53]
Polymer embedded titania	100	38	[54]
UiO-66	335	1624	This work
Form-UiO-66	296	1653	This work
UiO-66-NH$_2$	131	295	This work
UiO-66-NO$_2$	227	575	This work
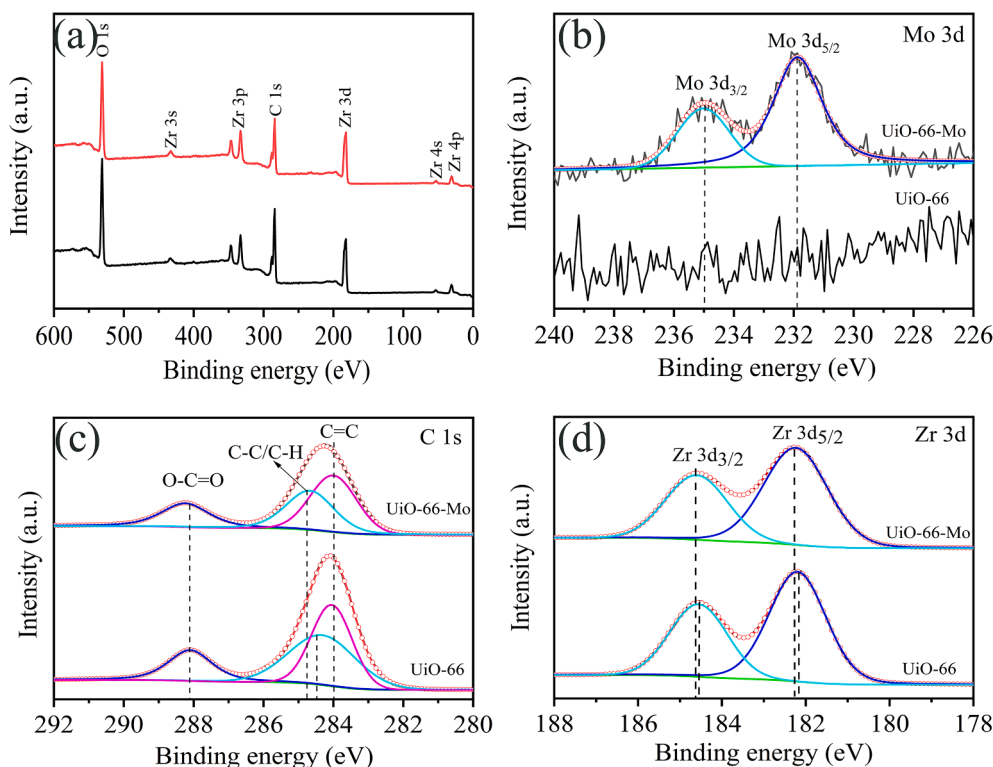
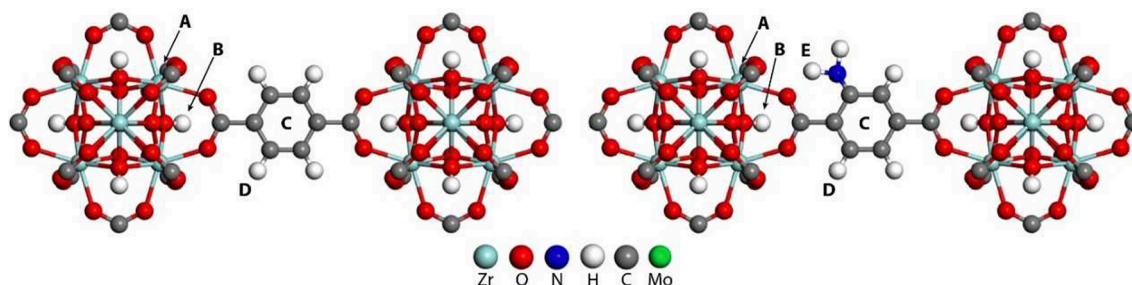**Fig. 4.** XPS spectra of UiO-66 before and after molybdenum adsorption (a) survey; (b) Mo 3d; (c) C 1s; (d) Zr 3d.

Fig. 5. Adsorption sites within the UiO-66 and UiO-66-NH$_2$ MOF structures

Table 2
Adsorption Sites and Energies (kJ mol^{-1}) (* refers to a configurational environment that combined with B, C and E sites).

MOFs	Mo species	Adsorption Sites and Energies in (kJ mol^{-1})				
		A	B	C	D	E
UiO-66	MoO_4^{2-}	-141	-130	+33	-25	-
	H_2MoO_4	-65/-56	-97	-65	-61	-
	$Mo_7O_{24}^{6-}$	-1539				
UiO-66-NH$_2$	MoO_4^{2-}	-155	-127	+10	-9	-73$^{(i)}$/-50$^{(ii)}$
	H_2MoO_4	-74	-101/-113*	-50	-73	-57

landscape both in the UiO-66 and UiO-66-NH$_2$ hosts. The relatively flat energy landscape indicates enhanced kinetics for the diffusion of the H$_2$MoO$_4$ species inside the MOF, allowing site accessibility for all the available material and thus enhancing the adsorption process. An interesting observation is that the H$_2$MoO$_4$ species does not necessarily chemically bind to the host structure due to its electrical neutrality. Nonetheless, it favourably adsorbs near the pore walls of the host

(Fig. S9 d-f) in a process that resembles more physio-sorption, which is also evident from the adsorption energy values obtained for positions A, C, D, and E in Table 2. However, the neutral H$_2$MoO$_4$ species, having the right size and orientation, can chemically adsorb to a binding spot that combines the configurational environment of the B, C and E sites (see Table 2). This favourable binding of −113 kJ mol^{-1} is depicted in Fig. S10, where the adsorbent creates bonds with the host structure of 2.36 Å (H—C), 1.88 Å (O—H) and, 1.93 Å (H—N).

Mo$_7$O$_{24}^{6-}$ species is a bulky anion, having dimensions of 0.97 by 0.49 nm. As a result, an important question is whether Mo$_7$O$_{24}^{6-}$ can intercalate within the host structure. DFT optimization of the UiO-66 hosts indicates an available pore size of 1.05 nm. By inserting Mo$_7$O$_{24}^{6-}$ within the host structure, we find a highly favourable binding environment (Table 2). This result is explained by the partial transformation of the host structure where some of the linkages are likely to react with the oxygen of the Mo$_7$O$_{24}^{6-}$ forming C—O—H bonds (Fig. S11). The Mo$_7$O$_{24}^{6-}$ molecule fits within the host, with most of the adsorbent's oxygen atoms being near the hydrogen atoms of the linkage molecules with distances between 2 and 2.4 Å. We also observe that the oxygen atoms of the adsorbent can successfully bind to C with an O-C bond of 1.43 Å. In the case of perfect alignment of Mo$_7$O$_{24}^{6-}$, an additional bond is created between O and Zr with a distance of 2.35 Å (Fig. 7). Further
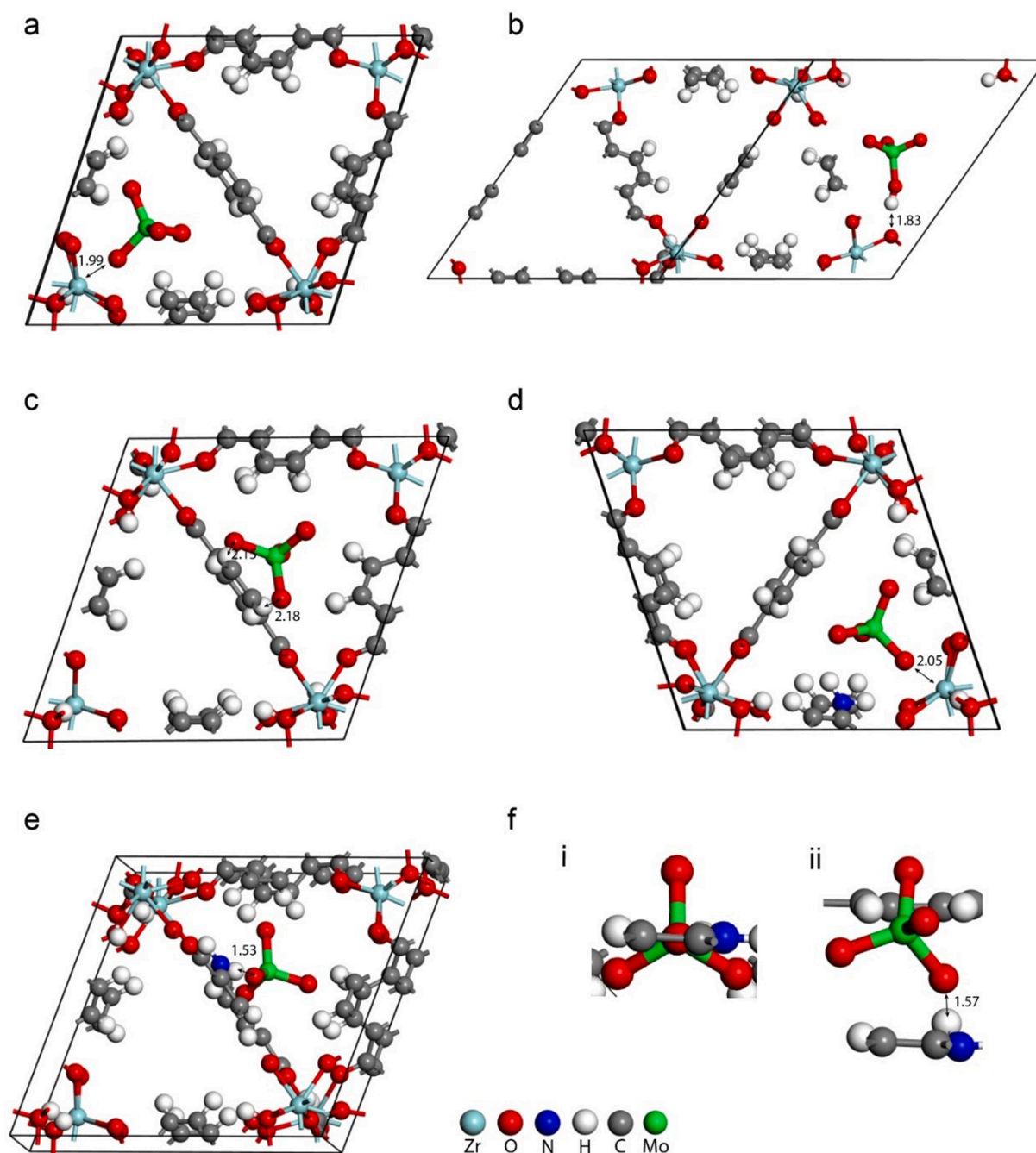
Fig. 6. Optimized structures of MoO$_4^{-2}$ adsorption within the UiO-66$_{sub}$host structure near a) position A b) position B, where we observe that the O-H of the Zr-O-H environment of the host breaks to form HMoO$_4^{-1}$, c) and position D. d) Optimized structures of MoO$_4^{-2}$ adsorption within the UiO-66-NH$_2$host structure near position A and e) position E. f) Difference between the two adsorption environments of adsorption near position E (i) −73 and (ii) −50 kJ/mol. All the interatomic distances indicated are in Å.

indications of the favourable environment created for Mo$_7$O$_{24}^{6-}$ adsorption are put forward by examining the predicted volume changes with DFT. The relaxed adsorption structures reveal a volume change of 6%. These values are definitely within the manageable range for mechanical stresses, especially for flexible materials such as MOFs.

Another important consideration is if the reaction kinetics allow these extremely favourable configurations to occur. The Mo$_7$O$_{24}^{6-}$ entering the main structure needs to diffuse through the side pores (~0.69 nm) of the MOF, which are considerably smaller. However, the linkers can rotate during motion, causing extended pores, this would be helpful for the penetration of molybdenum species [67,68]. Nevertheless, our calculations depict strong indications for favourable

adsorption, showing that the binding spots and coordination offered for the Mo$_7$O$_{24}^{6-}$ species lead to significantly lower energy (more stable) configurations when in the environment of the UiO-66 hosts. Certainly, there are also some other minor molybdenum species in solution, such as HMoO$^-$, H$_2$Mo$_6$O$_{21}^{4-}$, which have smaller sizes and would enter the porous structure more easily. Moreover, In the case of UiO-66-NO$_2$, the —NO$_2$ groups are also favourable for Mo adsorption and it has similar binding energy with the UiO-66-NH$_2$. Overall, molybdenum species can adsorb on the surface of Zr-based MOFs by electrostatic adsorption. The inner-sphere interaction between molybdenum species and adsorbents at several adsorption sites is enhanced through the Zr-O-Mo coordination, hydrogen bonds and π-anions.
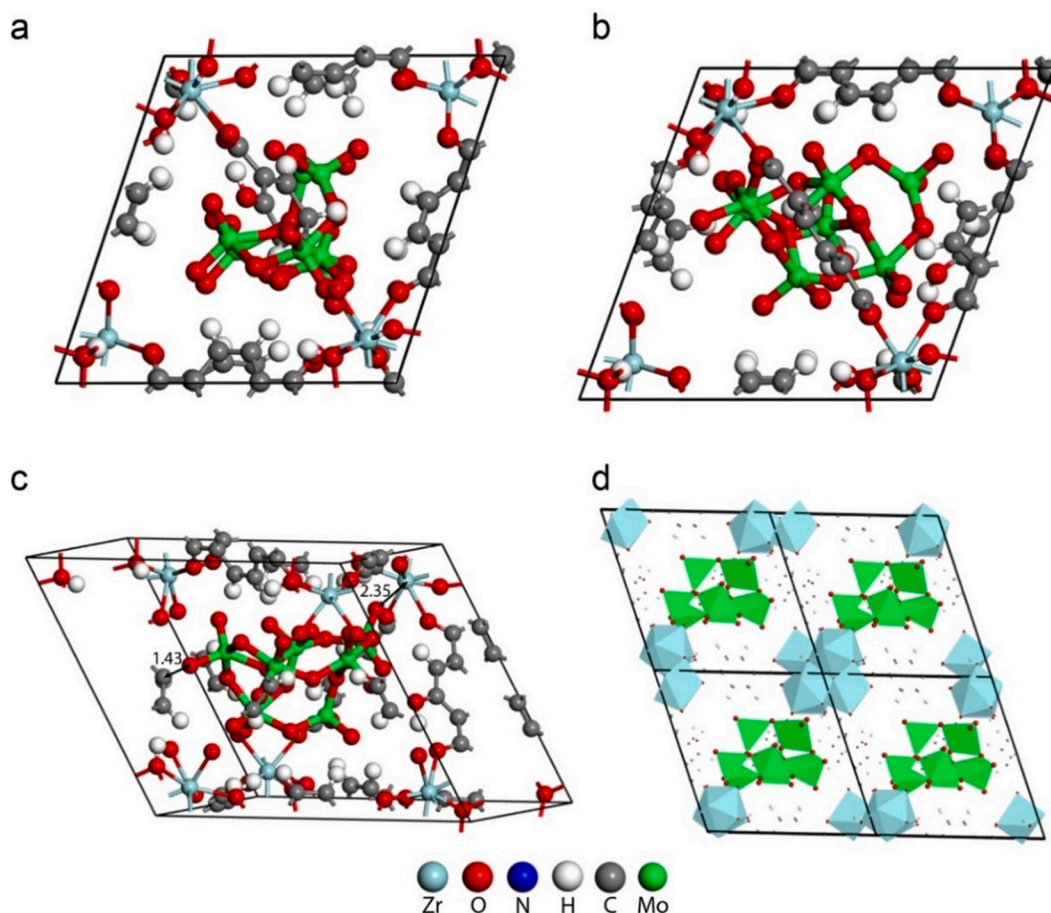
Zr   O   N   H   C   Mo

Fig. 7. Optimized structure from different angles of Mo$_7$O$_{24}$$^{-6}$ in the UiO-66 host.

3.4. Performance of Form-UiO-66 as adsorbent in ^{99}Mo/^{99m}Tc generator

In order to evaluate the performance of the prepared Zr-based MOFs as adsorbent in the ^{99}Mo/^{99m}Tc generator, Form-UiO-66 was selected due to its higher crystal purity, which allows it to be applied in a chromatographic column and continuous loading and elution. The dynamic molybdenum adsorption uptake of Form-UiO-66 was determined to be 203 mg g^{-1}, which is consistent with the adsorption results utilizing non-radioactive molybdenum. After removing the loosely adsorbed molybdenum ions by flushing the column with 0.9% saline solution, the practical dynamic adsorption capacity was determined to be 145 mg g^{-1}, which is consistent with the uptake value during fast adsorption process at low molybdenum concentration (See Fig. 3). In addition, this practical uptake is more than 7 times than that of conventional bulk alumina with an adsorption capacity in the range of 2–20 mg g^{-1}.

Subsequently, the column was eluted daily with saline solution for a period of 6 days and ^{99m}Tc elution efficiency was determined. Table 3 shows the elution results of the prepared column. It can be observed that

about 60% of ^{99m}Tc was eluted in the first two elutions and >70% of ^{99m}Tc was eluted in the following days. The Zr breakthrough in all elution fractions was below the detection limit of ICP-OES (<10 ppb). The presence of ^{99}Mo in the ^{99m}Tc eluted samples is about 1.2% in all elutions, which is higher than the limit of <0.1% as described in the International Pharmacopoeia (IP) [69]. The ^{99}Mo breakthrough may be associated with the size of the column used, which can lead to channel forming. These results prove that our adsorbents show good adsorption performance and chemical stability, while the elution performance of the column in the ^{99}Mo/^{99m}Tc generator needs to be optimized before clinical applications.

A generator based on 2 g of Form-UiO-66 as adsorbent could deliver 2 Ci ^{99}Mo activity if ^{99}Mo with a specific activity of 6.9 Ci g^{-1} of higher was utilized. The alternative methods to fission deliver ^{99}Mo with specific activities in the range of 1–10 Ci g^{-1} [2]. This clearly indicates the potential of MOFs as adsorbents in ^{99}Mo/^{99m}Tc based on LSA ^{99}Mo, which could provide an alternative to the current scenario and open the possibility of using many more production facilities worldwide.

4. Conclusions

In conclusion, this study showed that UiO-66 and its functionalized derivatives have great potential to be utilized as molybdenum adsorbents in ^{99}Mo/^{99m}Tc generator. The results reveal that UiO-66 and its functionalized derivatives exhibit outstanding Mo adsorption performance and that the maximum Mo adsorption capacity of UiO-66 can reach up to 335 mg g^{-1}, which is higher than most metal oxides for molybdenum adsorption. The adsorption mechanism was investigated by DFT, which indicates the interaction between MOFs and Mo species was affected by different binding such as Zr—O—Mo coordination,

Table 3
Elution parameters of the Form-UiO-66 in ^{99}Mo/^{99m}Tc generator over a period of 6 days.

Elution No.	Elution efficiency (%)	^{99}Mo breakthrough (%)	Zr breakthrough (ppm)
1	61.4	1.1	0
2	57.6	1.2	0
3	76.2	1.2	0
4	73.1	1.3	0
5	71.2	0.9	0
6	74.7	1.3	0

π-anions and hydrogen bonding. Moreover, DFT results proved that $Mo_7O_{24}^{6-}$ ions can be intercalated with the host structure by multiple binding sites. The Form-UiO-66 was successfully used for the $^{99}Mo/^{99m}Tc$ generator fabrication. The practical dynamic adsorption capacity of Form-UiO-66 was 145 mg g^{-1}, when a Mo concentration of 10 mg ml^{-1} was used. ^{99m}Tc can be eluted from the column within a 60–70% efficiency for 6 consecutive days without Zr breakthrough, but having ^{99}Mo breakthrough above the clinically allowed value. Therefore, UiO-66 MOFs have great potential for Mo adsorption and ^{99m}Tc elution in the $^{99}Mo/^{99m}Tc$ generator and a thorough study and optimization of the generator is under evaluation.

CRediT authorship contribution statement

Chao Ma: Methodology, Software, Validation, Formal analysis, Investigation, Data curation, Writing – original draft, Visualization. **Alexandros Vasileiadis:** Software, Writing – review & editing. **Hubert T. Wolterbeek:** Conceptualization. **Antonia G. Denkova:** Conceptualization, Supervision, Writing – review & editing. **Pablo Serra Crespo:** Conceptualization, Supervision, Writing – review & editing.

Declaration of Competing Interest

The authors declare that they have no known competing financial interests or personal relationships that could have appeared to influence the work reported in this paper.

Acknowledgments

Appendix A. Supplementary material

Supplementary data to this article can be found online at https://doi.org/10.1016/j.apsusc.2021.151340.

References

[1] D. Papagiannopoulou, Technetium-99m radiochemistry for pharmaceutical applications, J. Label. Compd. Radiopharm. 60 (11) (2017) 502–520.

[2] V.S. Le, Tc-99m generator development: up-to-date Tc-99m recovery technologies for increasing the effectiveness of Mo-99 utilisation, Sci. Technol. Nucl. Install. 2014 (2014) 1–41.

[3] G.C. Krijger, B. Ponsard, M. Harfensteller, H.T. Wolterbeek, J.W.F. Nijsen, The necessity of nuclear reactors for targeted radionuclide therapies, Trends Biotechnol. 31 (7) (2013) 390–396.

[4] M.R. Pillai, A. Dash, F.F. Knapp, Sustained availability of ^{99m}Tc: possible paths forward, J. Nucl. Med. 54 (2013) 313–323.

[5] E. National Academies of Sciences, Medicine opportunities and approaches for supplying molybdenum-99 and associated medical isotopes to global markets: proceedings of a symposium, National Academies Press, 2018.

[6] Thomas J. Ruth, The shortage of technetium-99m and possible solutions, Annu. Rev. Nucl. Part. Sci. 70 (1) (2020) 77–94.

[7] Andrew J. Einstein, Breaking america's dependence on imported molybdenum, JACC Cardiovasc Imaging. 2 (3) (2009) 369–371.

[8] J. Moret, J. Alkemade, T.M. Upcraft, E. Oehlke, H.T. Wolterbeek, J.R. van Ommen, A.G. Denkova, The application of atomic layer deposition in the production of sorbents for $^{99}Mo/^{99m}Tc$ generator, Appl. Radiat. Isot. 164 (2020) 109266.

[9] S. Hasan, M.A. Prelas, Molybdenum-99 production pathways and the sorbents for $^{99}Mo/^{99m}Tc$ generator systems using (n, γ) ^9Mo: A review, SN Appl. Sci. 2 (2020) 1782.

[10] M.R. Pillai, F.F. Knapp, Overcoming the ^{99m}Tc Shortage: Are Options Being Overlooked? J. Nucl. Med. 52 (2011) 15N.

[11] R. Chakravarty, R. Ram, A. Dash, M.R. Pillai, Preparation of clinical-scale $^{99}Mo/^{99m}Tc$ column generator using neutron activated low specific activity ^{99}Mo and nanocrystalline gamma-Al_2O_3 as column matrix, Nucl. Med. Biol. 39 (7) (2012) 916–922.

[12] I. Saptiama, Y.V. Kaneti, Y. Suzuki, K. Tsuchiya, N. Fukumitsu, T. Sakae, J. Kim, Y. M. Kang, K. Ariga, Y. Yamauchi, Template-free fabrication of mesoporous alumina nanospheres using post-synthesis water-ethanol treatment of monodispersed aluminum glycerate nanospheres for molybdenum adsorption, Small 14 (2018), e1800474.

[13] A.G. Denkova, B.E. Terpstra, O.M. Steinbach, J.T. Dam, H.T. Wolterbeek, Adsorption of molybdenum on mesoporous aluminum oxides for potential application in nuclear medicine, Sep. Sci. Technol. 48 (2013) 1331–1338.

[14] R. Chakravarty, R. Ram, R. Mishra, D. Sen, S. Mazumder, M.R.A. Pillai, A. Dash, Mesoporous alumina (MA) based double column approach for development of a clinical scale $^{99}Mo/^{99m}Tc$ generator using (n, γ) ^{99}Mo: An enticing application of nanomaterial, Ind. Eng. Chem. Res. 52 (2013) 11673–11684.

[15] S. Xiang, Y. He, Z. Zhang, H. Wu, W. Zhou, R. Krishna, B. Chen, Microporous metal-organic framework with potential for carbon dioxide capture at ambient conditions, Nat. Commun. 3 (2012) 954.

[16] P.G. Boyd, A. Chidambaram, E. Garcia-Diez, C.P. Ireland, T.D. Daff, R. Bounds, A. Gladysiak, P. Schouwink, S.M. Moosavi, M.M. Maroto-Valer, J.A. Reimer, J.A. R. Navarro, T.K. Woo, S. Garcia, K.C. Stylianou, B. Smit, Data-driven design of metal-organic frameworks for wet flue gas CO_2 capture, Nature. 576 (2019) 253–256.

[17] E. Lopez-Maya, C. Montoro, V. Colombo, E. Barea, J.A.R. Navarro, Improved CO_2 capture from flue gas by basic sites, charge gradients, and missing linker defects on nickel face cubic centered MOFs, Adv. Func. Mater. 24 (2014) 6130–6135.

[18] Long Jiao, Yang Wang, Hai-Long Jiang, Qiang Xu, Metal-organic frameworks as platforms for catalytic applications, Adv. Mater. 30 (37) (2018) 1703663, https://doi.org/10.1002/adma.v30.3710.1002/adma.201703663.

[19] L. Zhu, X.Q. Liu, H.L. Jiang, L.B. Sun, Metal-organic frameworks for heterogeneous basic catalysis, Chem. Rev. 117 (2017) 8129–8176.

[20] Nagy L. Torad, Ming Hu, Shinsuke Ishihara, Hiroaki Sukegawa, Alexis A. Belik, Masataka Imura, Katsuhiko Ariga, Yoshio Sakka, Yusuke Yamauchi, Direct synthesis of MOF-derived nanoporous carbon with magnetic Co nanoparticles toward efficient water treatment, Small. 10 (10) (2014) 2096–2107.

[21] B. Li, J.Q. Zheng, J.Z. Guo, C.Q. Dai, A novel route to synthesize MOFs-derived mesoporous dawsonite and application in elimination of Cu(II) from wastewater, Chem. Eng. J. 383 (2020), 123174.

[22] M.X. Wu, Y.W. Yang, Metal-organic framework (MOF)-based drug/cargo delivery and cancer therapy, Adv. Mater. 29 (2017) 1606134.

[23] Isabel Abánades Lázaro, Ross S. Forgan, Application of zirconium MOFs in drug delivery and biomedicine, Coord. Chem. Rev. 380 (2019) 230–259.

[24] Li-Li Tan, Haiwei Li, Yue Zhou, Yuanyuan Zhang, Xiao Feng, Bo Wang, Ying-Wei Yang, Zn^{2+}-Triggered drug release from biocompatible zirconium MOFs equipped with supramolecular gates, Small. 11 (31) (2015) 3807–3813.

[25] I. Abanades Lazaro, C.J.R. Wells, R.S. Forgan, Multivariate modulation of the Zr-MOF UiO-66 for defect-controlled combination anticancer drug delivery, Angew. Chem. Int. Ed. Engl. 59 (2020) 5211–5217.

[26] P. Silva, S.M. Vilela, J.P. Tome, F.A. Almeida Paz, Multifunctional metal-organic frameworks: from academia to industrial applications, Chem. Soc. Rev. 44 (2015) 6774–6803.

[27] C.Y. Lee, O.K. Farha, B.J. Hong, A.A. Sarjeant, S.T. Nguyen, J.T. Hupp, Light-harvesting metal-organic frameworks (MOFs): efficient strut-to-strut energy transfer in bodipy and porphyrin-based MOFs, J. Am. Chem. Soc. 133 (2011) 15858–15861.

[28] Pawan Kumar, Akash Deep, Ki-Hyun Kim, Metal organic frameworks for sensing applications, Trac-Trend, Anal. Chem. 73 (2015) 39–53.

[29] J. Li, X. Wang, G. Zhao, C. Chen, Z. Chai, A. Alsaedi, T. Hayat, X. Wang, Metal-organic framework-based materials: superior adsorbents for the capture of toxic and radioactive metal ions, Chem. Soc. Rev. 47 (2018) 2322–2356.

[30] J. Canivet, A. Fateeva, Y. Guo, B. Coasne, D. Farrusseng, Water adsorption in MOFs: fundamentals and applications, Chem. Soc. Rev. 43 (2014) 5594–5617.

[31] Nicholas C. Burtch, Himanshu Jasuja, Krista S. Walton, Water stability and adsorption in metal-organic frameworks, Chem. Rev. 114 (20) (2014) 10575–10612.

[32] Mathivathani Kandiah, Merete Hellner Nilsen, Sandro Usseglio, Søren Jakobsen, Unni Olsbye, Mats Tilset, Cherif Larabi, Elsje Alessandra Quadrelli, Francesca Bonino, Karl Petter Lillerud, Synthesis and stability of tagged UiO-66 Zr-MOFs, Chem. Mater. 22 (24) (2010) 6632–6640.

[33] A.J. Howarth, Y. Liu, P. Li, Z. Li, T.C. Wang, J.T. Hupp, O.K. Farha, Chemical, thermal and mechanical stabilities of metal–organic frameworks, Nat. Rev. Mater. 1 (2016) 15018.

[34] C.G. Piscopo, A. Polyzoidis, M. Schwarzer, S. Loebbecke, Stability of UiO-66 under acidic treatment: Opportunities and limitations for post-synthetic modifications, Microporous Mesoporous Mater. 208 (2015) 30–35.

[35] M. Amin, M.A. El-Amir, H.E. Ramadan, H. El-Said, $^{99}Mo/^{99m}Tc$ generators based on aluminum molybdate gel matrix prepared by nano method, J. Radioanal. Nucl. Chem. 318 (2018) 915–922.

[36] Yalan Wang, Nan Zhang, Danni Chen, Dan Ma, Guoguang Liu, Xuegang Zou, Yuping Chen, Ranjun Shu, Qingyun Song, Wenying Lv, Facile synthesis of acid-modified UiO-66 to enhance the removal of Cr(VI) from aqueous solutions, Sci. Total. Environ. 682 (2019) 118–127.

[37] John P. Perdew, Kieron Burke, Matthias Ernzerhof, Generalized gradient approximation made simple, Phys. Rev. Lett. 77 (18) (1996) 3865–3868.

[38] G. Kresse, J. Furthmüller, Efficiency of Ab-initio total energy calculations for metals and semiconductors using a Plane-Wave Basis set, Comput. Mater. Sci. 6 (1) (1996) 15–50.

[39] P.E. Blochl, Projector Augmented-Wave method, Phys. Rev. B Condens. Matter. 50 (1994) 17953–17979.

[40] S. Grimme, J. Antony, S. Ehrlich, H. Krieg, A consistent and accurate Ab Initio parametrization of density functional dispersion correction (DFT-D) for the 94 elements H-Pu, J. Chem. Phys. 132 (2010) 154104.

[41] M.K. Aydinol, A.F. Kohan, G. Ceder, K. Cho, J. Joannopoulos, Ab Initio study of lithium intercalation in metal oxides and metal dichalcogenides, Phys. Rev. B 56 (1997) 1354–1365.

[42] J. Wei, W. Zhang, W. Pan, C. Li, W. Sun, Experimental and theoretical investigations on Se(IV) and Se(VI) adsorption to UiO-66-Based metal–organic frameworks, Environ. Sci.: Nano 5 (2018) 1441–1453.

[43] Hussein Rasool Abid, Ha Ming Ang, Shaobin Wang, Effects of ammonium hydroxide on the structure and gas adsorption of nanosized Zr-MOFs (UiO-66), Nanoscale. 4 (10) (2012) 3089, https://doi.org/10.1039/c2nr30244f.

[44] P. Yang, Q. Liu, J. Liu, H. Zhang, Z. Li, R. Li, L. Liu, J. Wang, Interfacial growth of a metal–organic framework (UiO-66) on functionalized graphene oxide (GO) as a suitable seawater adsorbent for extraction of uranium (VI), J. Mater. Chem. A 5 (2017) 17933–17942.

[45] Paul C. Lemaire, Dennis T. Lee, Junjie Zhao, Gregory N. Parsons, Reversible low-temperature metal node distortion during atomic layer deposition of Al_2O_3 and TiO_2 on UiO-66-NH_2 metal–organic framework crystal surfaces, ACS Appl. Mater. Interfaces. 9 (26) (2017) 22042–22054.

[46] Maria N. Timofeeva, Valentina N. Panchenko, Jong Won Jun, Zubair Hasan, Maria M. Matrosova, Sung Hwa Jhung, Effects of linker substitution on catalytic properties of porous zirconium terephthalate UiO-66 in acetalization of benzaldehyde with methanol, Appl. Catal. A-Gen 471 (2014) 91–97.

[47] Hira Saleem, Uzaira Rafique, Robert P. Davies, Investigations on post-synthetically modified UiO-66-NH_2 for the adsorptive removal of heavy metal ions from aqueous solution, Microporous Mesoporous Mater. 221 (2016) 238–244.

[48] A. Davantès, G. Lefèvre, In situ real time infrared spectroscopy of sorption of (poly) molybdate ions into layered double hydroxides, J. Phys. Chem. A. 117 (48) (2013) 12922–12929.

[49] J. Serrano Gómez, F. Granados Correa, ^{99m}Tc generator with hydrated MnO_2 as adsorbent of ^{99}Mo, J. Radioanal. Nucl. Chem. 254 (2002) 625–628.

[50] Q. Qazi, M. Ahmad, Preparation and evaluation of hydrous titanium oxide as a high affinity adsorbent for molybdenum (^{99}Mo) and its potential for use in ^{99m}Tc generators, Radiochim. Acta. 99 (2011) 231–235.

[51] Indra Saptiama, Yusuf Valentino Kaneti, Hamid Oveisi, Yoshitaka Suzuki, Kunihiko Tsuchiya, Kimiko Takai, Takeji Sakae, Subrata Pradhan, Md. Shahriar A. Hossain, Nobuyoshi Fukumitsu, Katsuhiko Ariga, Yusuke Yamauchi, Molybdenum adsorption properties of alumina-embedded mesoporous silica for medical radioisotope production, Bull. Chem. Soc. Jpn. 91 (2) (2018) 195–200.

[52] T.W. Fasih, T.M. Sakr, R.R. Ayoub, M. Amin, Preparation and evaluation of nano-crystalline titania as sorbent for ^{99}Mo/^{99m}Tc generator, Sep. Sci. Technol. 51 (2016) 2115–2121.

[53] R. Chakravarty, R. Ramu, D. Ashutosh, Comparative assessment of nanostructured metal oxides: A potential step forward to develop clinically useful ^{99}Mo/^{99m}Tc generators using (n, γ) ^{99}Mo, Sep. Sci. Technol. 49 (2014) 1825–1837.

[54] R. Chakravarty, R. Shukla, S. Gandhi, R. Ram, A. Dash, M. Venkatesh, A.K. Tyagi, Polymer embedded nanocrystalline titania sorbent for ^{99}Mo/^{99m}Tc generator, J. Nanosci. Nanotechnol. 8 (2008) 4447–4452.

[55] Xiangyang Zhu, Bing Li, Jian Yang, Yongsheng Li, Wenru Zhao, Jianlin Shi, Jinlou Gu, Effective adsorption and enhanced removal of organophosphorus

[56] Nguyen Tien Thao, Nguyen Duc Trung, Dang Van Long, Activity of molybdate-intercalated layered double hydroxides in the oxidation of styrene with air, Catal. Lett. 146 (5) (2016) 918–928.

[57] Liang Huang, Jingwei Xiang, Wei Zhang, Chaoji Chen, Henghui Xu, Yunhui Huang, 3D interconnected porous $NiMoO_4$ nanoplate arrays on Ni foam as high-performance binder-free electrode for supercapacitors, J. Mater. Chem. A 3 (44) (2015) 22081–22087.

[58] Debasis Ghosh, Soumen Giri, Chapal Kumar Das, Synthesis, characterization and electrochemical performance of graphene decorated with 1D $NiMoO_4$•n H_2O nanorods, Nanoscale. 5 (21) (2013) 10428, https://doi.org/10.1039/c3nr02444j.

[59] Jie Xu, Sha He, Hualei Zhang, Jiancai Huang, Huaxiang Lin, Xuxu Wang, Jinlin Long, Layered metal–organic framework/graphene nanoarchitectures for organic photosynthesis under visible light, J. Mater. Chem. A 3 (48) (2015) 24261–24271.

[60] Jian Yang, Yan Dai, Xiangyang Zhu, Zhe Wang, Yongsheng Li, Qixin Zhuang, Jianlin Shi, Jinlou Gu, Metal–organic frameworks with inherent recognition sites for selective phosphate sensing through their coordination-induced fluorescence enhancement effect, J. Mater. Chem. A. 3 (14) (2015) 7445–7452.

[61] Caiqin Chen, Dezhi Chen, Shasha Xie, Hongying Quan, Xubiao Luo, Lin Guo, Adsorption behaviors of organic micropollutants on zirconium metal-organic framework UiO-66: analysis of surface interactions, ACS Appl. Mater. Interfaces. 9 (46) (2017) 41043–41054.

[62] J.J. Cruywagen, Protonation, Oligomerization, and Condensation Reactions of Vanadate(V), Molybdate(VI), and Tungstate(VI), Adv. Inorg. Chem. 49 (1999) 127–182.

[63] C. Tian, J. Zhao, J. Ou, J. Wan, Y. Cai, Z. Lin, Z. Dang, B. Xing, Enhanced adsorption of P-Arsanilic acid from water by amine-modified UiO-67 as examined using extended X-Ray absorption fine structure, X-Ray photoelectron spectroscopy, and density functional theory calculations, Environ. Sci. Technol. 52 (2018) 3466–3475.

[64] R.J. Drout, K. Otake, A.J. Howarth, T. Islamoglu, L. Zhu, C. Xiao, S. Wang, O. K. Farha, Efficient capture of perrhenate and pertechnetate by a mesoporous Zr metal–organic framework and examination of anion binding motifs, Chem. Mater. 30 (2018) 1277–1284.

[65] O.B. Berryman, V.S. Bryantsev, D.P. Stay, D.W. Johnson, B.P. Hay, Structural criteria for the design of anion receptors: the interaction of halides with electron-deficient arenes, J. Am. Chem. Soc. 129 (2007) 48–58.

[66] Vyacheslav S. Bryantsev, Benjamin P. Hay, Are C-H Groups significant hydrogen bonding sites in anion receptors? benzene complexes with Cl⁻, NO_3^-, and ClO_4^-, J. Am. Chem. Soc. 127 (23) (2005) 8282–8283.

[67] Joshua T. Damron, Jialiu Ma, Ricardo Kurz, Kay Saalwächter, Adam J. Matzger, Ayyalusamy Ramamoorthy, The influence of chemical modification on linker rotational dynamics in metal-organic frameworks, Angew. Chem. Int. Ed. Engl. 57 (28) (2018) 8678–8681.

[68] Wojciech Danowski, Thomas van Leeuwen, Shaghayegh Abdolahzadeh, Diederik Roke, Wesley R. Browne, Sander J. Wezenberg, Ben L. Feringa, Unidirectional rotary motion in a metal-organic framework, Nat. Nanotechnol. 14 (5) (2019) 488–494.

[69] Sodium Pertechnetate (99mTc) Injection (Non-Fission): Final text for addition to the International Pharmacopoeia, World Health Organization Document, 2009.